The Astrophysical Journal, 866:41 (10pp), 2018 October 10 https://doi.org/10.3847/1538-4357/aadadf

Coexistence of Slow-mode and Alfvén-mode Waves and Structures in 3D Compressive MHD Turbulence

Liping Yang[1,2,3], Lei Zhang[1], Jiansen He[2,3], Chuanyi Tu[2], Shengtai Li[4], Xin Wang[5], and Linghua Wang[2]
[1] SIGMA Weather Group, State Key Laboratory for Space Weather, National Space Science Center, Chinese Academy of Sciences, 100190, Beijing, People's Republic of China
[2] School of Earth and Space Sciences, Peking University, 100871 Beijing, People's Republic of China; jshept@pku.edu.cn
[3] HIT Institute of Space Science and Applied Technology, 518055, Shenzhen, People's Republic of China
[4] Theoretical Division, MS B284, Los Alamos National Laboratory, Los Alamos, NM 87545, USA
[5] School of Space and Environment, Beihang University, 100191 Beijing, People's Republic of China
Received 2018 January 11; revised 2018 August 11; accepted 2018 August 14; published 2018 October 8

Abstract

The compressible component of solar wind turbulence displays a slow-mode feature. However, the nature of the slow-mode fluctuations remain open. In this work, based on numerical simulations of the driven compressible magnetohydrodynamic (MHD) turbulence with a uniform mean magnetic field, we use polarization of the MHD modes to decompose turbulent velocity and magnetic fields into Alfvén modes, slow modes, and fast modes. The numerical results with different cross-helicity, plasma beta β, and Alfvén Mach number note that fast modes are a marginal component among the three decomposed modes, and the compressible component of the MHD turbulence behaves mainly as the slow modes. Both of the decomposed slow modes and Alfvén modes exhibit a Kolmogorov-like power-law spectrum and evident anisotropy, with wavevectors mainly distributing around the directions perpendicular to the uniform mean field. For the first time, it is found that the propagating slow magnetosonic waves as well as the non-propagating slow-mode structures are combined to contribute to the compressible fluctuations, and the propagating Alfvén waves as well as the non-propagating Alfvén-mode structures coexist for the non-compressible fluctuations. However, there is unlikely a one-to-one match between the identified slow waves and Alfvén waves, or between the identified slow-mode structures and Alfvén-mode structures. These findings provide a new perspective on our understanding of the compressible and non-compressible fluctuations.

Key words: magnetohydrodynamics (MHD) – methods: numerical – solar wind – turbulence

1. Introduction

The solar wind is permeated by various kinds of propagating waves and convective structures (Tu & Marsch 1995; Bruno & Carbone 2013). A complex mixture of compressible and incompressible fluctuations is involved in the solar wind turbulence, with compressible fluctuations usually as a minor but significant component. The compressibility of solar wind fluctuations usually manifests itself as a slow-mode nature (Burlaga 1968; Marsch & Tu 1993; Tu & Marsch 1994; Hnat et al. 2005; Kellogg & Horbury 2005; Yao et al. 2011, 2013a, 2013b; Howes et al. 2012; Klein et al. 2012; Zhao et al. 2014; He et al. 2015; Narita & Marsch 2015; Shi et al. 2015, 2017; Wang et al. 2016; Verscharen et al. 2017). As the quasi-parallel slow-mode magnetosonic waves are believed to be strongly damped, e.g., can be damped to be less than $1/e$ of original amplitude within three wavelengths of propagation in the solar corona (Ruan et al. 2016), the slow-mode-like compressible fluctuations have often been interpreted as pressure-balanced structures (PBSs; Tu & Marsch 1995). On the basis of the Helios data, Tu & Marsch (1994) found an anticorrelation between magnetic pressure and thermal pressure for fluctuations at inertial range scales of solar wind turbulence. Kellogg & Horbury (2005) studied small-scale density oscillations in the solar wind and recognized that the PBSs they found are simply ion acoustic waves in a perpendicular propagation limit. Using a large statistical set of measurements from the *Wind* spacecraft, Howes et al. (2012) showed that the compressible component of inertial range solar wind turbulence is primarily in the category of kinetic slow-mode. Recently, the study of Verscharen et al. (2017) suggests that the large-scale compressive fluctuations in the solar wind behave more fluid-like than kinetic slow-mode-like. However, as far as we know, it has no answer about the true nature of the slow-mode fluctuations in the inertial range of the solar wind. Are they just propagating waves or just convected structures? The velocity fluctuation can be invoked beside the density and magnetic field perturbations to identify the longitudinal compression/expansion, which are the drivers of the energy propagation for slow modes (He et al. 2015).

Meanwhile, the question of the origin of slow-mode waves and convected structures is still open. Both waves and structures could be generated in the sub-Alfvénic flow region near the Sun (Liu et al. 2014), and subsequently propagate through or are passively advected by the solar wind into the interplanetary medium (Tu & Marsch 1995; Borovsky 2008; Zank et al. 2017). On the other hand, as the relative amplitudes of the compressible fluctuations in the solar wind show no prominent radial evolution, both waves and structures are suggested to be locally produced and replenished by the nonlinear evolution or energy cascade of turbulence (Roberts et al. 1992; Tu & Marsch 1993; Bruno et al. 2001).

Apart from the observational evidences, numerical simulations of magnetohydrodynamic (MHD) turbulence have been conducted to understand the behaviors of the compressive fluctuations, with many of them focusing on the statistical properties of compressible modes (Cho & Lazarian 2002, 2003; Passot & Vázquez-Semadeni 2003; Vestuto et al. 2003; Cho & Lazarian 2005; Hnat et al. 2005; Kowal et al. 2007;

Kowal & Lazarian 2010; Brandenburg & Lazarian 2013; Yang et al. 2015, 2017a, 2017b, 2017c; Zhang et al. 2015a, 2015b; Yoon et al. 2016; Shi et al. 2017). The spectral properties and/or anisotropy of slow modes in MHD turbulence were shown to be a Kolmogorov $k^{-5/3}$ spectrum and scale-dependent Goldreich–Sridhar anisotropy, with slow modes passively imitating Alfvén modes, while fast modes have a $k^{-3/2}$ spectrum and isotropy (Cho & Lazarian 2003). The intermittency of the different MHD modes was shown to be very different, and the high-order statistics of compressible motions clearly depended on the sonic and Alfvénic Mach number (Kowal & Lazarian 2010). At the same time, the local behaviors of MHD slow modes are discussed. Zhang et al. (2015a) identified slow wave trains from the simulation of MHD turbulence, and provided a description of their evolution and possible interaction with other types of MHD waves. Yang et al. (2017a) found the existence of multiscale PBSs in MHD turbulence as well as their likely production by the perpendicular cascade of highly oblique-propagating slow-mode waves. Yet the true nature and origin of the slow-mode component of the MHD turbulence still remains to be understood. These questions will be studied here by an analysis of the numerical results of the driven MHD turbulence with a uniform mean magnetic field. Specifically, the polarizations of the MHD modes are used to decompose turbulent velocity and magnetic fields into slow modes, Alfvén modes, and fast modes; the propagation of the decomposed slow modes and Alfvén modes are investigated in detail.

2. Numerical MHD Model

The details of the three-dimensional (3D) numerical MHD model have been described in Yang et al. (2017a). Here, we describe its basic aspects and modifications for the current study. The description of the plasma is given by compressible MHD governing equations, which involve a fluctuating flow velocity, $\boldsymbol{u}(x, y, z, t)$, magnetic field, $\boldsymbol{b}(x, y, z, t)$, density, $\rho(x, y, z, t)$, and temperature, $T(x, y, z, t)$. A uniform mean magnetic field, $\boldsymbol{B}_0 = (0, 0, 1)$, is imposed in the z-direction. The numerical MHD model solves the conservation of mass, momentum, and energy together with the induction equation as

$$\frac{\partial \rho}{\partial t} + \nabla \cdot (\rho \boldsymbol{u}) = 0, \tag{1}$$

$$\frac{\partial \rho \boldsymbol{u}}{\partial t} + \nabla \cdot \left[\rho \boldsymbol{u}\boldsymbol{u} + \left(p + \frac{1}{2}\boldsymbol{B}^2\right)\boldsymbol{I} - \boldsymbol{B}\boldsymbol{B}\right] = \nu \nabla^2 \boldsymbol{u} + \rho(\boldsymbol{f}_1 - \boldsymbol{f}_2), \tag{2}$$

$$\frac{\partial e}{\partial t} + \nabla \cdot \left[\boldsymbol{u}\left(e + p + \frac{1}{2}\boldsymbol{B}^2\right) - (\boldsymbol{u} \cdot \boldsymbol{B})\boldsymbol{B}\right] = \nabla \cdot (\boldsymbol{u} \cdot \nu \nabla \boldsymbol{u}) + \nabla \cdot (\boldsymbol{B} \times \eta \boldsymbol{j}) + \rho \boldsymbol{u} \cdot (\boldsymbol{f}_1 - \boldsymbol{f}_2) + \boldsymbol{B} \cdot (\boldsymbol{f}_1 + \boldsymbol{f}_2), \tag{3}$$

$$\frac{\partial \boldsymbol{B}}{\partial t} + \nabla \cdot (\boldsymbol{u}\boldsymbol{B} - \boldsymbol{B}\boldsymbol{u}) = \eta \nabla^2 \boldsymbol{B} + \boldsymbol{f}_1 + \boldsymbol{f}_2, \tag{4}$$

with $e = (1/2)\rho \boldsymbol{u}^2 + p/(\gamma - 1) + (1/2)\boldsymbol{B}^2$, $\boldsymbol{j} = \nabla \times \boldsymbol{B}$ corresponding to the total energy density and current density, respectively. Here, ρ is the mass density, p is the thermal pressure, $\boldsymbol{B} = \boldsymbol{B}_0 + \boldsymbol{b}$ denotes the total magnetic field, t is time, $\gamma = 5/3$ is the adiabatic index, $\nu = 0.0001$ is the viscosity, and $\eta = 0.0001$ is the magnetic resistivity, respectively.

The large-scale random drivers $\boldsymbol{f}_1$ and $\boldsymbol{f}_2$ are applied in Fourier space and then are transformed back into real space (Cho & Lazarian 2003; Yang et al. 2017a). At each time moment, the components of $\boldsymbol{f}_1$ and $\boldsymbol{f}_2$ are defined in Fourier space as $Pm(\boldsymbol{k})\exp(i\phi)$, where ϕ is the uniform-distributed random phase angle between $[0, 2\pi]$. $Pm(\boldsymbol{k})$ is isotropic in $\boldsymbol{k}$-space and consists of 21 Fourier components with a wavenumber of $k \leqslant 3.5$. The amplitude of each Fourier component is a constant plus a small noise. $\boldsymbol{f}_1$ and $\boldsymbol{f}_2$ satisfy $\nabla \cdot \boldsymbol{f}_1 = 0$ and $\nabla \cdot \boldsymbol{f}_2 = 0$, respectively. An example of their space and temporal behaviors is shown in Yang et al. (2017a). To introduce cross-helicity (indicator of imbalance), the amplitude of $\boldsymbol{f}_1$ is designed to be not equal to that of $\boldsymbol{f}_2$.

For a snapshot in time, the turbulent velocity fields are decomposed into three MHD eigenmodes, i.e., fast, slow, and Alfvén, in the Fourier space, which are defined in the reference frame related to the mean magnetic field $\boldsymbol{B}_0$. For a given wavevector $\boldsymbol{k}$, the three MHD mode velocities

$$\delta \boldsymbol{v}_{\rm FM} \sim v_{\rm p,F}^2 \hat{\boldsymbol{k}} - v_{\rm A}^2 \cos\theta \hat{\boldsymbol{B}}_0, \tag{5}$$

$$\delta \boldsymbol{v}_{\rm SM} \sim v_{\rm p,S}^2 \hat{\boldsymbol{k}} - v_{\rm A}^2 \cos\theta \hat{\boldsymbol{B}}_0, \tag{6}$$

$$\delta \boldsymbol{v}_{\rm AM} \sim \hat{\boldsymbol{k}} \times \hat{\boldsymbol{B}}_0, \tag{7}$$

form an orthogonal coordinate system (Marsch 1986; Zhang et al. 2015a). In Equations (5)–(6), $v_{\rm p,F}$, $v_{\rm p,S}$, as well as $v_{\rm A}$ are the phase speed of the fast and slow magnetosonic waves as well as Alfvén waves, $\hat{\boldsymbol{k}}$ is the unit vector along the wavevector $\boldsymbol{k}$, $\hat{\boldsymbol{B}}_0$ is the unit vector along the mean magnetic field $\boldsymbol{B}_0$, and θ is the angle between $\hat{\boldsymbol{k}}$ and $\hat{\boldsymbol{B}}_0$. The perturbation speeds, corresponding to fast ($\boldsymbol{u}_{\rm FM}(\boldsymbol{k})$), slow ($\boldsymbol{u}_{\rm SM}(\boldsymbol{k})$), and Alfvén ($\boldsymbol{u}_{\rm AM}(\boldsymbol{k})$) modes are computed via projections $\boldsymbol{u}(\boldsymbol{k})$ into these three perturbation directions. Please note that $\boldsymbol{u}(\boldsymbol{k})$ is assumed to be the superposition of velocity fluctuations of the three MHD modes.

According to the magnetic fields of the fast ($\delta \boldsymbol{b}_{\rm FM}$), slow ($\delta \boldsymbol{b}_{\rm SM}$), and Alfvén ($\delta \boldsymbol{b}_{\rm AM}$) modes (Marsch 1986; Zhang et al. 2015a), we obtain perturbation magnetic fields of fast ($\boldsymbol{b}_{\rm FM}(\boldsymbol{k})$), slow ($\boldsymbol{b}_{\rm SM}(\boldsymbol{k})$), and Alfvén ($\boldsymbol{b}_{\rm AM}(\boldsymbol{k})$) modes for the MHD turbulence by

$$\boldsymbol{b}_{\rm FM}(\boldsymbol{k}) = \frac{\boldsymbol{u}_{\rm FM}(\boldsymbol{k})}{\delta \boldsymbol{v}_{\rm FM}} \delta \boldsymbol{b}_{\rm FM}, \tag{8}$$

$$\boldsymbol{b}_{\rm SM}(\boldsymbol{k}) = \frac{\boldsymbol{u}_{\rm SM}(\boldsymbol{k})}{\delta \boldsymbol{v}_{\rm SM}} \delta \boldsymbol{b}_{\rm SM}, \tag{9}$$

$$\boldsymbol{b}_{\rm AM}(\boldsymbol{k}) = \frac{\boldsymbol{u}_{\rm AM}(\boldsymbol{k})}{\delta \boldsymbol{v}_{\rm AM}} \delta \boldsymbol{b}_{\rm AM}. \tag{10}$$

After the above decomposition of the MHD turbulence into three modes, we conduct inverse Fourier transform to get the perturbation velocities and magnetic fields of the three modes in real space.

To choose a particular time series for the mode analysis above, the following criterion is used: the trace power spectral densities (PSDs) of the velocity and magnetic field are maintained to change little.

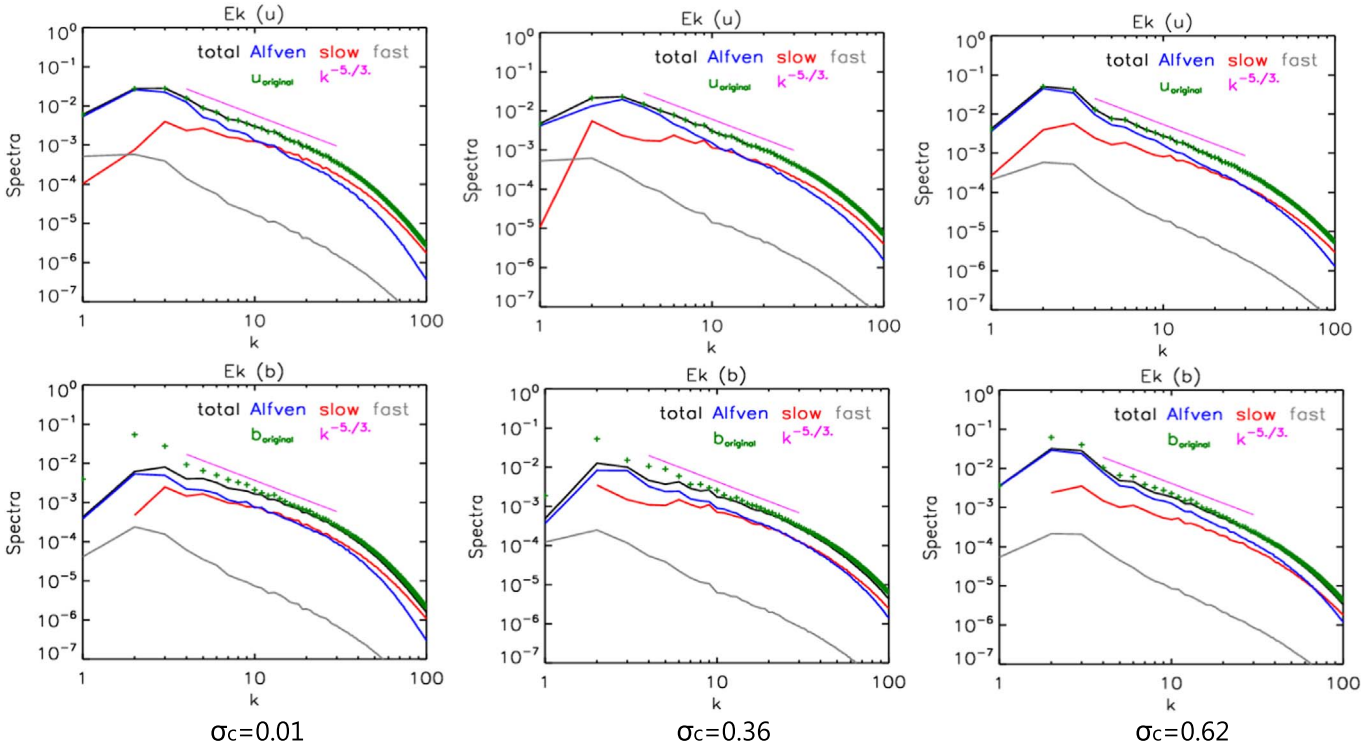

Figure 1. Spectra of Alfvén modes (blue), slow modes (red), fast modes (gray), total modes (black, Alfvén modes+slow modes+fast modes), and original data (green crosses) of the velocity (***u***, upper panels) and magnetic field (***b***, lower panels) when $\sigma_c = 0.01$, $\sigma_c = 0.36$, and $\sigma_c = 0.62$. For reference, a Kolmogorov-like power-law spectrum is plotted as the purple lines.

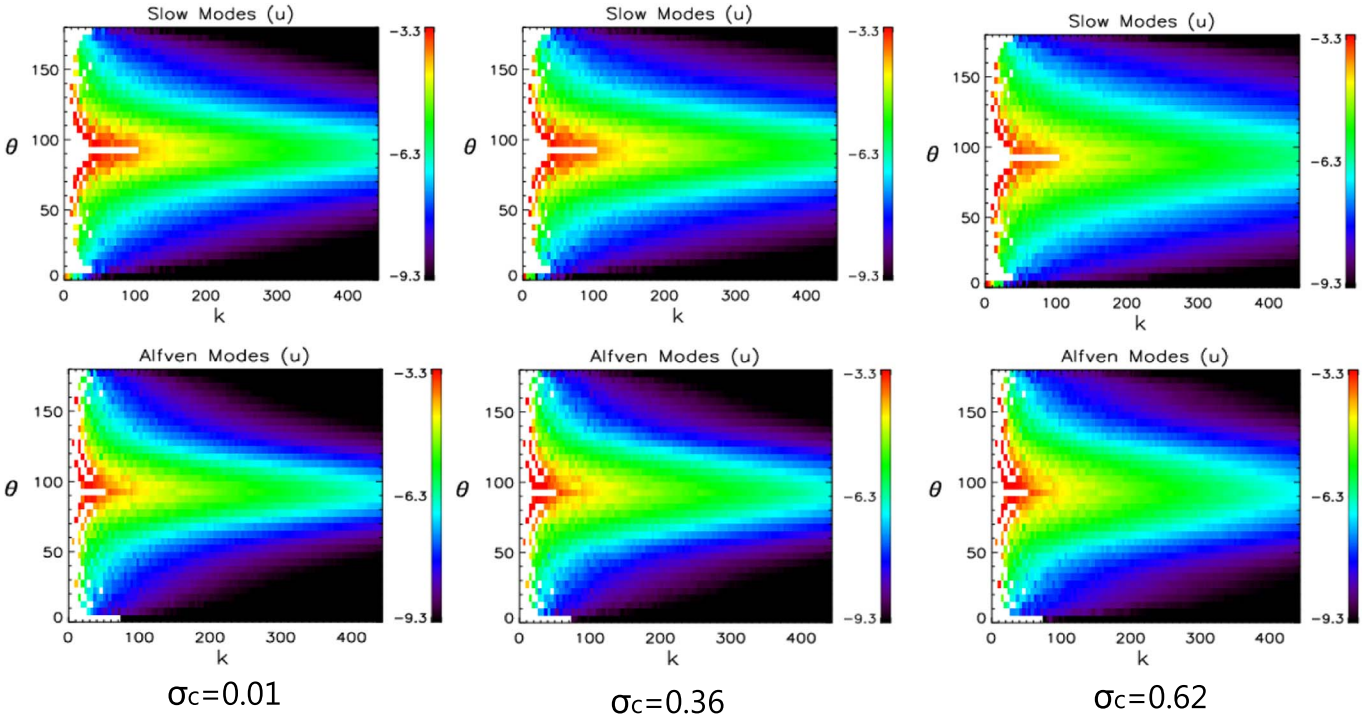

Figure 2. Distributions of power spectral densities (PSDs) of the slow-mode velocity (top panels) and the Alfvén-mode velocity (bottom panels) on the $k - \theta$ plane when $\sigma_c = 0.01$, $\sigma_c = 0.36$, and $\sigma_c = 0.62$. Note that PSDs are in log scale, and the white color on the color map means there is no data in the corresponding $k - \theta$ bin.

3. Numerical Results

Here, we present numerical results with different cross-helicity, plasma beta β, and Alfvén Mach number M_A. The results of runs with altered parameters are based on a basic case, in which rms amplitudes of the magnetic field ($B_{\rm rms}$) and velocity ($u_{\rm rms}$) are maintained to be approximately 0.39 and 0.41, the normalized cross-helicity (σ_c) is about 0.62, the plasma beta β is about 1.50, Mach number ($u_{\rm rms}/C_s$) is about

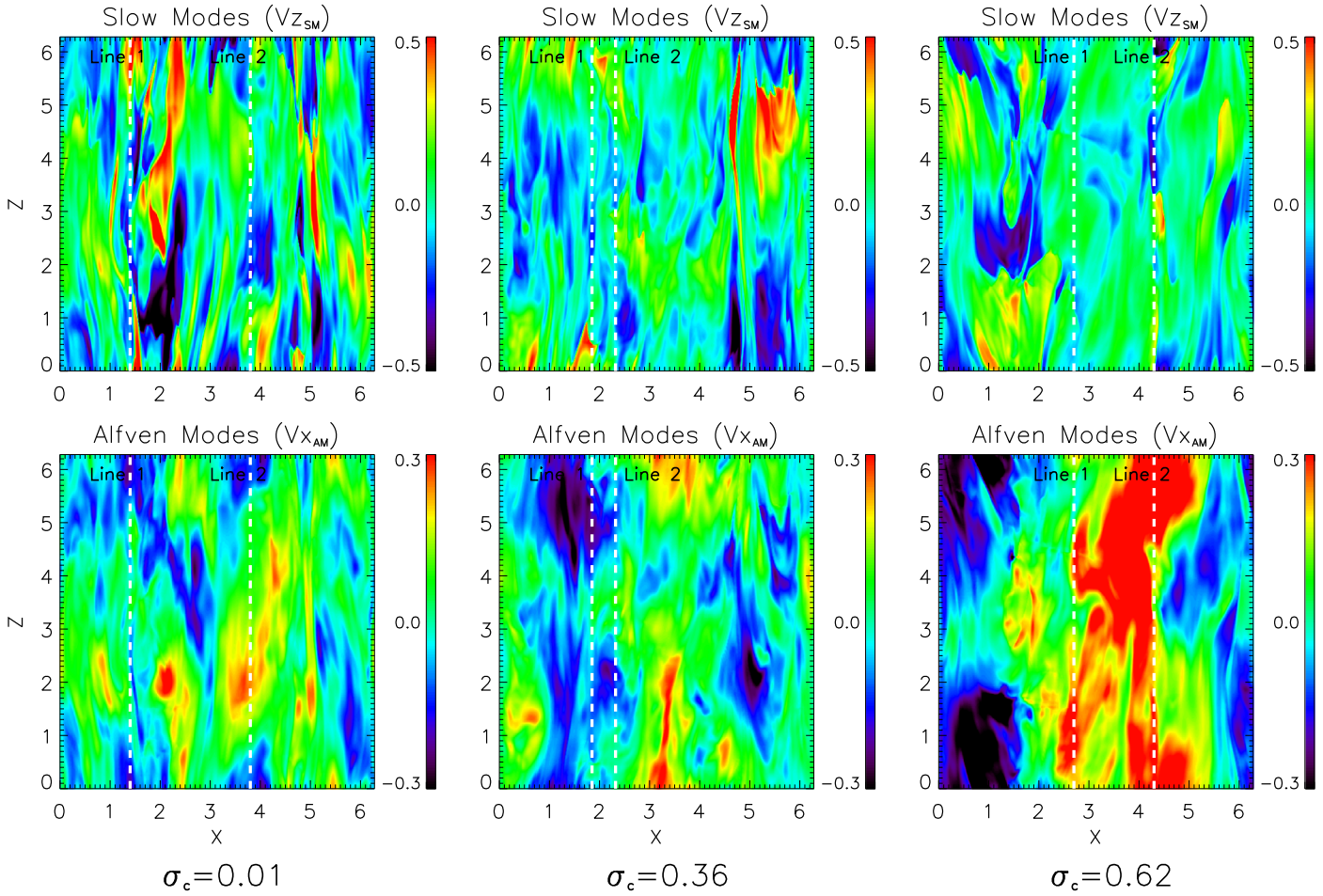

Figure 3. Distributions of the z-component of the slow-mode velocity ($Vz_{\rm SM}$, upper panels) and the x-component of Alfvén-mode velocity ($Vx_{\rm AM}$, lower panels) in the $y = 4.93$ plane when $\sigma_c = 0.01$, $\sigma_c = 0.36$, and $\sigma_c = 0.62$. The white dashed lines define the selected lines (Line 1 and Line 2) for the propagation speed analysis.

0.32, and Alfvén Mach number ($u_{\rm rms}/V_A$) is 0.41, where C_s(=1.21) and V_A (=1.00) are the sonic speed and Alfvén speed, respectively. Relative to the basic case, a parameter is adjusted in each run. It should be noted that the parameters, such as cross-helicity, plasma beta β, Alfvén Mach number M_A, and so on, are measured at the time slice used for the analysis.

Figure 1 shows the spectra of velocity ($\boldsymbol{u}$, upper panels) and magnetic field ($\boldsymbol{b}$, lower panel) for Alfvén modes (blue), slow modes (red), and fast modes (gray) when $\sigma_c = 0.01$ (left panels), $\sigma_c = 0.36$ (middle panels), and $\sigma_c = 0.62$ (right panels). In this figure, the spectra of the total modes, whose PSDs are the sums of those of Alfvén modes, slow modes, and fast modes, are shown as the black lines; the original spectra of the velocity ($\boldsymbol{u}$) and magnetic field ($\boldsymbol{b}$) are presented as the green crosses; and a Kolmogorov-like power-law spectrum is plotted as the purple lines for reference. It can be seen that for the velocity and magnetic field, the spectra of both Alfvén modes and slow modes exhibit comparable PSDs, while the fast modes are only a marginal component among the three modes. The spectrum of the total modes follow a Kolmogorov spectrum. For the velocity, the spectrum of the total modes completely coincides with the original spectrum. For the magnetic field, the spectrum of the total modes keeps the same trend with the original spectrum, and the PSDs of the total modes are nearly equal to those of the original magnetic field, except those at the energy-injection region, which peaks at $k = 2$ and terminates at $k = 3.5$. As the cross-helicity σ_c increases, this approximate equality between $Ek(b)$ for total modes and for the original data is more evident.

Figure 2 give the distributions of the PSDs of the slow-mode velocity (top panels) and the Alfvén-mode velocity (bottom panels) on the $k - \theta$ plane when $\sigma_c = 0.01$ (left panels), $\sigma_c = 0.36$ (middle panels), and $\sigma_c = 0.62$ (right panels). It can be seen that the PSDs of both the slow modes and the Alfvén modes mainly concentrate around the wavevectors perpendicular to the mean field $\boldsymbol{B}_0$. With the increase of the wavenumber k, the condensate is more evident, which means that their energies mainly lie at quasi-perpendicular propagations. It should be noted that in this figure the slow modes and the Alfvén modes with $\theta > 90°$ do not associate with the inverse-propagation waves as we only conduct 3D (x, y, z) Fourier transformations without making the temporal Fourier transform.

Figure 3 presents the distributions of the z-component of the slow-mode velocity ($Vz_{\rm SM}$, upper panels) and the x-component of Alfvén-mode velocity ($Vx_{\rm AM}$, lower panels) in the $y = 4.93$ plane when $\sigma_c = 0.01$ (left panels), $\sigma_c = 0.36$ (middle panels), and $\sigma_c = 0.62$ (right panels). As the oscillations of the slow modes along the z-direction are dominant over those along the x- and y-directions, and the oscillations of the Alfvén modes along the x- and y-directions are equivalent, here we just show the z-component of the slow-mode velocity and the x-component of Alfvén-mode velocity for illustration. It can be seen that in real space, the oscillation patterns of both the slow

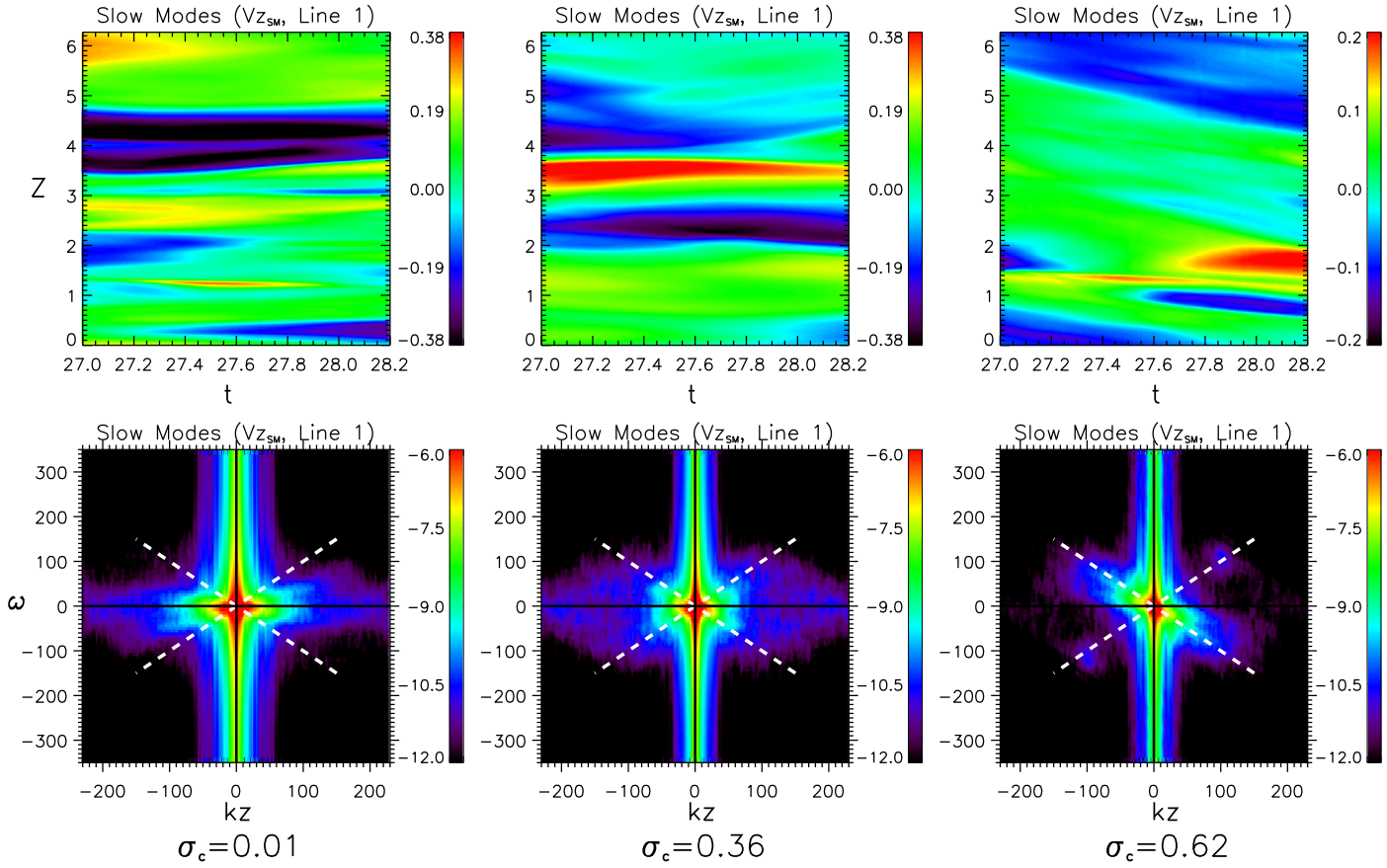

Figure 4. Distance–time ($Z-t$) diagrams (upper panels) and wavenumber–frequency ($k_z-\omega$) diagrams (lower panels) of the slow-mode velocity ($Vz_{\rm SM}$) along Line 1 shown in Figure 3 when $\sigma_c = 0.01$, $\sigma_c = 0.36$, and $\sigma_c = 0.62$. The white dashed lines show the theoretical dispersion relation of slow magnetosonic wave $\omega_{\rm SM}(k_z)$. Note that the PSDs are in log scale.

modes and the Alfvén modes tend to preferentially align along the direction of the uniform mean field.

To analyze the nature of the decomposed slow modes and Alfvén modes, we extract the values of the slow-mode velocity and the Alfvén-mode velocity along the direction of the mean field $\boldsymbol{B}_0$ shown as Line 1 and Line 2 in Figure 3, and stack the obtained profiles in time sequence. This gives the distance–time ($Z-t$) diagrams as displayed in the upper panels of Figures 4–7. To determine whether the slow-mode velocity and the Alfvén-mode velocity follow the dispersion relation of the slow magnetosonic wave and the Alfvén wave, respectively, we use the obtained distance–time diagrams and conduct the spatial-temporal Fourier analysis of them. This gives wavenumber–frequency ($k_z-\omega$) diagrams of the slow-mode velocity and the Alfvén-mode velocity as shown in the lower panels of Figures 4–7. The white dashed lines in Figures 4 and 6 denote the theoretical dispersion relation of slow magnetosonic wave $\omega_{\rm SM}(k_z)$, which reads as $\omega_{\rm SM}/k_z = v_{\rm p,S}/\cos(\theta) \approx \min(Cs, V_A)$ (Zhang et al. 2015a). The white dashed lines in Figures 5 and 7 denote the theoretical dispersion relation of Alfvén wave $\omega_{\rm AM}(k_z)$, which reads as $\omega_{\rm AM}/k_z = V_A$. It should be noted that in these figures the slow-mode velocity and the Alfvén-mode velocity are extracted along the same lines.

Figure 4 shows that along Line 1, the decomposed slow-mode velocities display no evident characteristic propagation speed for the three cases. Although their distance–time diagrams display stripes resulting from the fronts of the decomposed slow-mode velocities, most of the stripes possess no obvious slopes. The corresponding wavenumber–frequency diagrams also give no clear relationship between wavenumber (k_z) and frequency (ω). Whether it is for the small k_z or the large k_z, the high power region of the decomposed slow modes mainly lies near $\omega = 0$, indicating that most of the decomposed slow-mode velocities along Line 1 are non-propagating parts of the perturbations.

Figure 5 shows that for the cases of $\sigma_c = 0.01$ and $\sigma_c = 0.36$, the decomposed Alfvén-mode velocities along Line 1 do not possess an evident characteristic propagation speed, which points out that most of the decomposed Alfvén-mode velocities along Line 1 behave as non-propagating Alfvén-mode perturbations. However, for the case of $\sigma_c = 0.62$, most of the decomposed Alfvén-mode velocities along Line 1 have an evident propagating speed, which coincides with the phase speed of Alfvén wave, indicating that most of the decomposed Alfvén-mode velocities along Line 1 for this case behave as Alfvén waves.

Figure 6 displays distance–time ($Z-t$) diagrams and wavenumber–frequency ($k_z-\omega$) diagrams of the slow-mode velocity ($Vz_{\rm SM}$) for Line 2 shown in Figure 3. From Figure 6, we can see that the decomposed slow-mode velocities along Line 2 display completely different propagating features from those along Line 1. The distance–time diagrams show the steep, recurrent stripes, but most of the stripes have obvious slopes. The slopes of these stripes correspond to the propagating speeds of the decomposed slow-mode velocities. The corresponding wavenumber–frequency diagrams show that the slow wave dispersion cross lines match well with the high

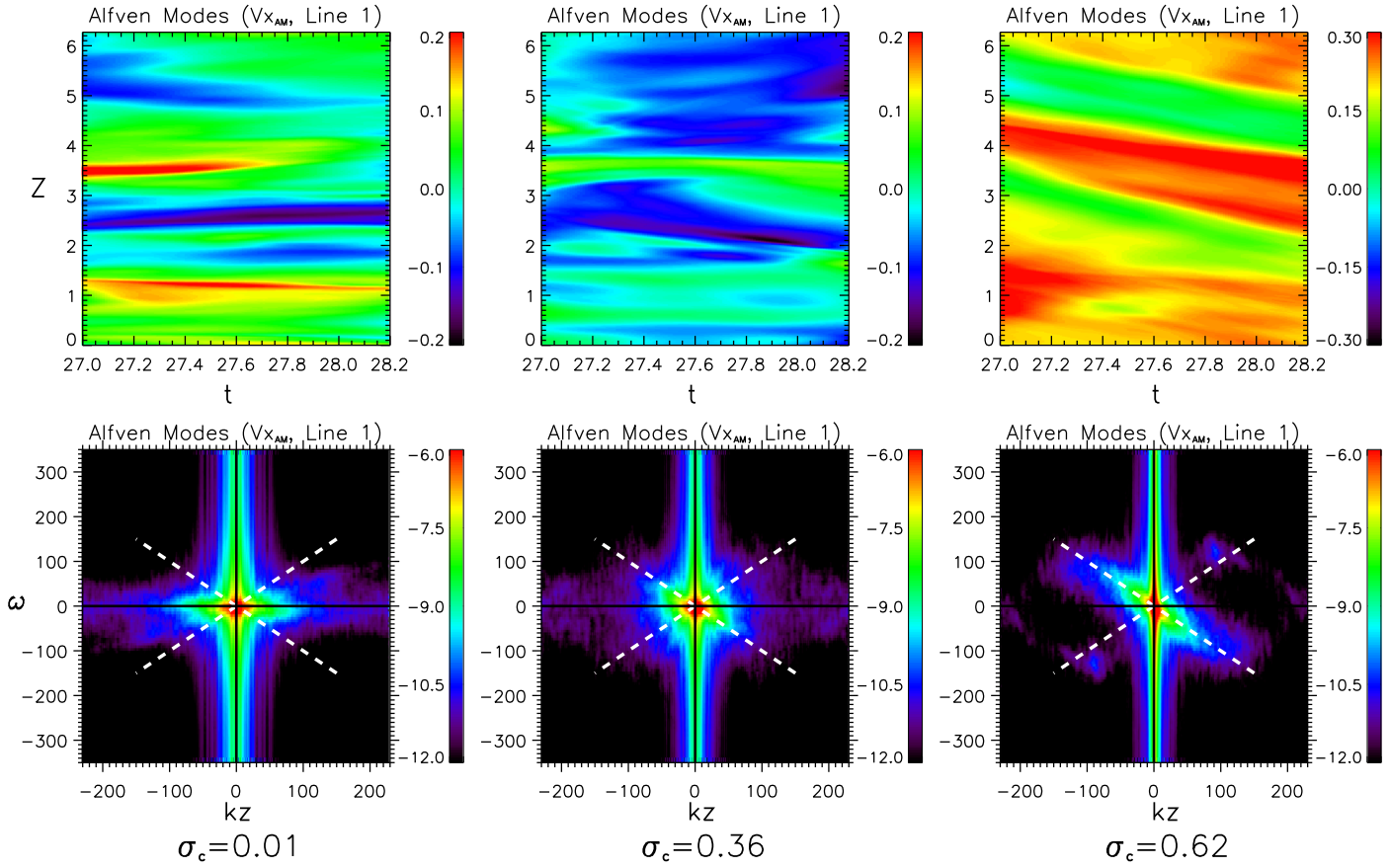

Figure 5. Same as Figure 4, but for the Alfvén-mode velocity ($Vx_{\rm AM}$). The white dashed lines show the theoretical dispersion relation of Alfvén wave $\omega_{\rm AM}(k_z)$.

power region of the decomposed slow-mode velocities, which is a clear signature of the existence of slow magnetosonic waves. Also, counter-propagating slow-mode waves are more prone to be seen when the cross-helicity σ_c decreases. As the wavevectors of the slow-mode velocity concentrates around the perpendicular direction, it can be said that the slow magnetosonic waves identified here are mainly quasi-perpendicular propagating.

Figure 7 shows that unlike the slow-mode velocities along Line 2, the Alfvén-mode velocities along the same line have no evident characteristic propagation pattern for $\sigma_c = 0.01$, while their propagation conforms well to the dispersion curve of Alfvén waves when $\sigma_c = 0.25$ and $\sigma_c = 0.62$. Also, as the wavevectors of the Alfvén-mode velocity concentrate around the perpendicular direction, the identified Alfvén waves can be said to be mainly quasi-perpendicular propagating.

To see how the above analyses are influenced by plasma beta β and Alfvén Mach number M_A, we also give the results of runs with $\beta = 0.15$, $\beta = 8.32$, $M_A = 0.12$, and $M_A = 0.58$ for the basic case of $\sigma_c = 0.62$. Figure 8 shows the spectra of Alfvén modes, slow modes, fast modes, total modes, and original data of velocity and magnetic field. It can be seen that the fast modes are only a small contribution to the total modes, although their contribution increases with the decrease of plasma beta β and the increase of Alfvén Mach number M_A. For the slow modes, their contribution to total modes changes largely with different plasma beta β but slightly with M_A. When plasma beta β is above 1, except in the energy-injection region, the slow-mode amplitudes are comparable to the Alfvén-mode amplitudes for both the velocity and magnetic field fluctuations. When plasma beta β becomes smaller than 1, the slow modes become important with the decrease of the scale for the velocity fluctuations, while they are a marginal component of the total modes for the magnetic field fluctuation.

The distance–time diagrams and wavenumber–frequency diagrams of the slow-mode velocity ($Vz_{\rm SM}$) and the Alfvén-mode velocity ($Vx_{\rm AM}$) for $\beta = 0.15$, $\beta = 8.32$, $M_A = 0.12$, and $M_A = 0.58$ give that both propagating and non-propagating parts of the slow-mode and Alfvén-mode perturbations also coexist. For the identified non-propagating slow-mode perturbations, the Alfvén modes along the same line can behave as non-propagating or propagating perturbations. For the identified slow-mode waves, the Alfvén modes along the same line can also behave as non-propagating or propagating perturbations.

To illustrate the correlations among the propagating compressive perturbations and among the propagating non-compressive perturbations, Figure 9 presents the distance–time diagrams of the propagating compressive perturbations Vz, Bz, B, and ρ (upper panels), and non-compressive perturbations $Vx_{\rm AM}$, $Bx_{\rm AM}$, $Vy_{\rm AM}$, and $By_{\rm AM}$ (lower panels), respectively. In this figure, the white dashed lines show the theoretical propagation speed of slow magnetosonic waves and Alfvén waves along the z-direction. The compressive perturbations and non-compressive perturbations are along different slices. It can be seen that for the propagating compressive perturbations, Vz is positively correlated with Bz, and Vz is also positively correlated with B, and the magnetic field intensity B is in negative correlation with the density ρ. Also, their propagation speed along the z-direction is the predicted propagation speed

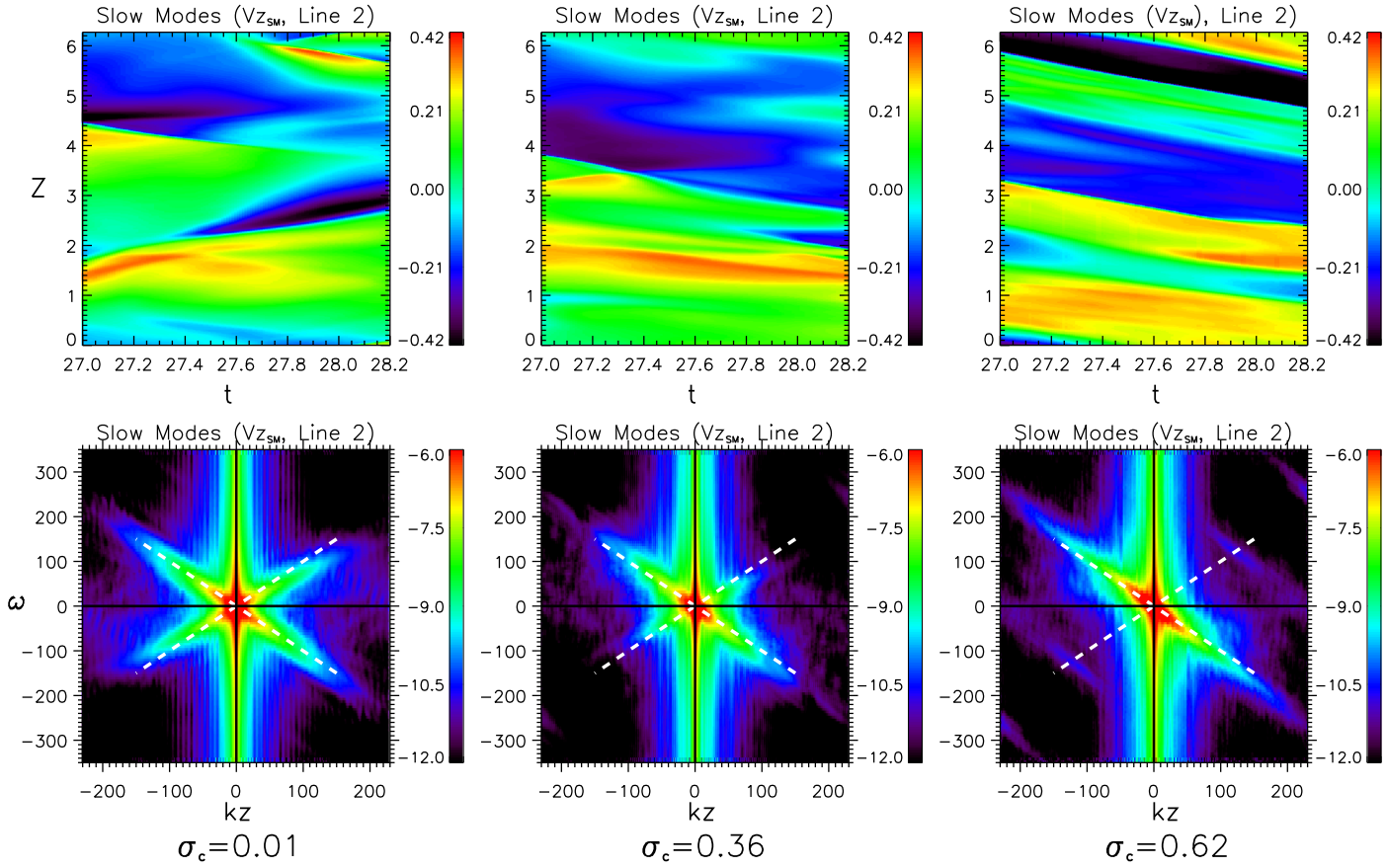

Figure 6. Distance–time ($Z - t$) diagrams (upper panels) and wavenumber–frequency ($k_z - \omega$) diagrams (lower panels) of the slow-mode velocity (Vz_{SM}) along Line 2. The white dashed lines show the theoretical dispersion relation of slow magnetosonic wave $\omega_{SM}(k_z)$. Note that the PSDs are in log scale. It can be seen that the oblique stripes in the distance–time diagrams (upper panels) are in line with the dispersion relation of oblique slow-mode waves as illustrated in the lower panels.

of slow magnetosonic waves. Thus, it is verified that these propagating compressive perturbations are anti-propagating slow magnetosonic waves. For the propagating non-compressive perturbations, Vx_{AM} and Bx_{AM}, with the nearly same values, are in positive correlation, and Vy_{AM} and By_{AM}, with the nearly same values, are also in positive correlation. Their propagation speed along the z-direction is the predicted propagation speed of Alfvén waves, noting that these propagating non-compressive perturbations are anti-propagating Alfvén waves.

To see whether the non-propagating compressive and non-compressive perturbations are structures, we first conduct four-dimensional (4D) spatial-temporal (x, y, z, t) Fourier transformations of the whole computational domain, and then filter with frequency $\omega = 0$, and finally conduct inverse Fourier transformations to get the pure non-propagating perturbations distributed in real space. Figure 10 displays the distance–time diagrams of the filtered compressive perturbations Vz, Bz, B, and ρ (upper panels) and non-compressive perturbations Vx_{AM}, Bx_{AM}, Vy_{AM}, and By_{AM} (lower panels). This figure shows that the filtered compressive perturbations are satisfied with the polarity relation of slow magnetosonic waves, and the filtered non-compressive perturbations conform to the polarity relation of Alfvén waves, thus verifying that these non-propagating compressive and non-compressive perturbations are slow-mode and Alfvén-mode structures, respectively.

As the total-energy-conserving equation is used in the current simulations, constant driving will result in constant accumulation of internal energy. To see how much the internal energy increases, Figure 11 presents the evolution of internal energy from $t = 0$ to $t = 30$ for the basic case. It can be seen that there is a quick increase of the internal energy from $t = 0$ to $t = 1.2$, and afterwards it rises slowly.

4. Summary and Discussion

In this work, based on the simulation results of the driven compressible MHD turbulence with a uniform mean magnetic field, we analyze the nature of the slow modes and Alfvén modes and do a comparison between them. The following statistical results are present: (1) the compressible component of the MHD turbulence is mainly in the slow modes with a Kolmogorov-like power-law spectrum; (2) the slow-mode and Alfvén-mode perturbations show evident anisotropy, with the wavevectors mainly distributing around the perpendicular directions; (3) the slow-mode perturbations can behave as the propagating slow magnetosonic waves and the non-propagating slow-mode structures; (4) the Alfvén-mode perturbations consist of the propagating Alfvén waves and the non-propagating Alfvén-mode structures; (5) there is an unlikely one-to-one match between the identified slow waves and Alfvén waves, or between the identified slow-mode structures and Alfvén-mode structures; and (6) for both the slow modes and the Alfvén modes, the generation in the vicinity of the wavevectors perpendicular to the uniform mean field is more effective than that near the wavevectors parallel to the uniform mean field.

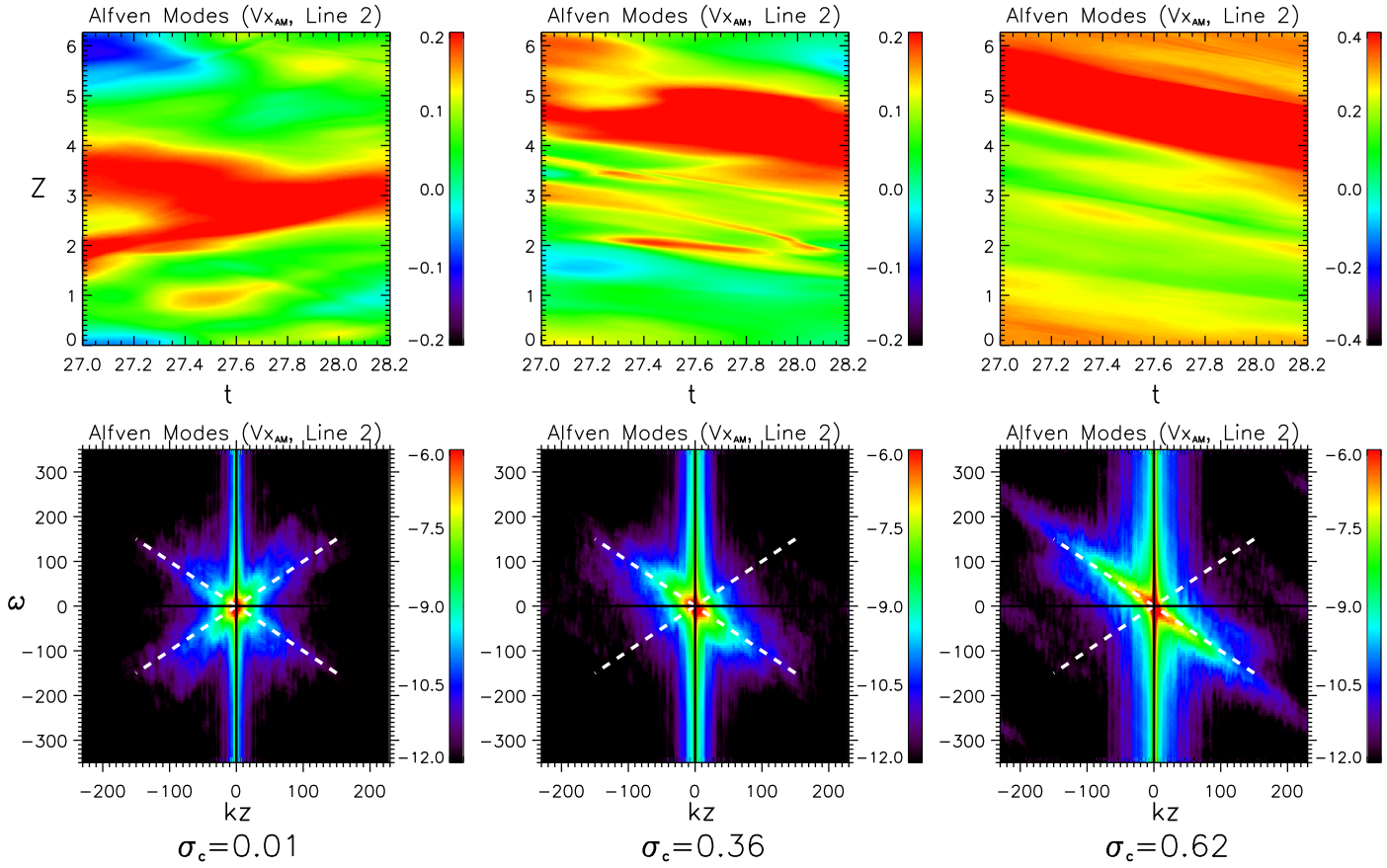

Figure 7. Same as Figure 6, but for the Alfvén-mode velocity ($Vx_{\rm AM}$). The white dashed lines show the theoretical dispersion relation of Alfvén wave $\omega_{\rm AM}(k_z)$.

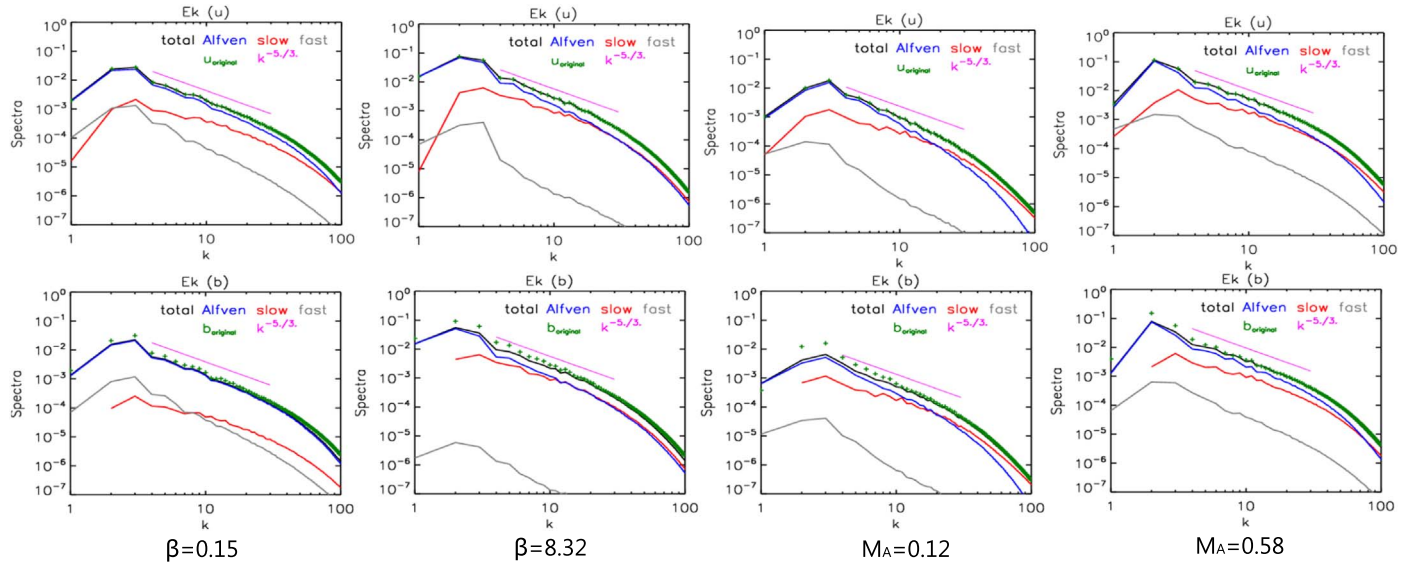

Figure 8. Same as Figure 1, but when $\beta = 0.15$, $\beta = 8.32$, $M_A = 0.12$, and $M_A = 0.58$.

Figures 1 and 8 also show that at the energy-injection region, $k < 3.5$, fluctuations behave as Alfvén modes, and slow modes are not effectively injected. Therefore, it is hard for slow modes themselves to cascade from energy-injection scales to smaller scales, and slow modes are prone to be produced directly from Alfvén modes.

However, along with these findings, there are some challenges and limitations. The dynamics in the solar wind plasma are largely collisionless, and there are some debates about whether MHD theories are invalid for the solar wind. Employing the linear Vlasov–Maxwell dispersion relation for a fully ionized proton and electron plasma, Klein et al. (2012) show that the MHD three wave modes have kinetic counterparts in a collisionless plasma that have properties similar to the MHD modes at large scales. The solar wind observations show that the typical dependence of cross-correlation between proton

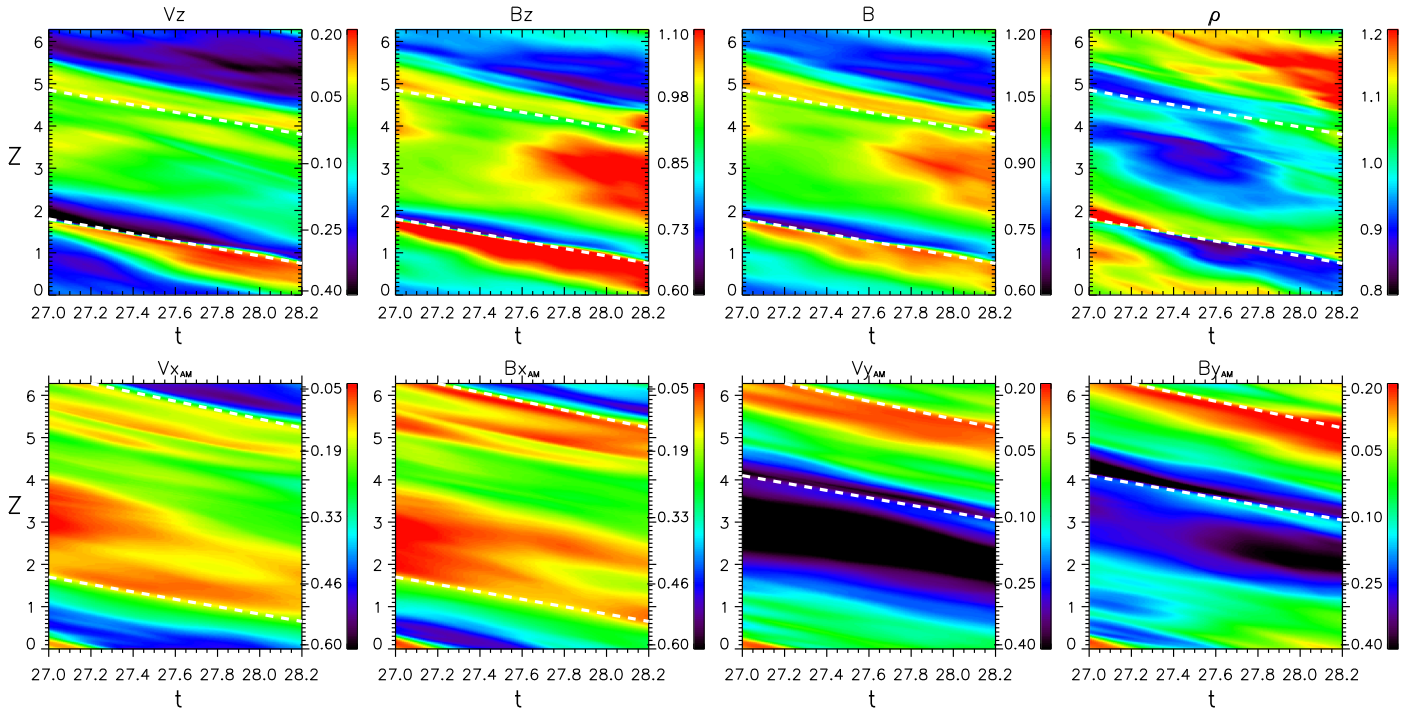

Figure 9. Distance–time ($Z - t$) diagrams of the propagating compressive perturbations Vz, Bz, B, and ρ (upper panels) and the propagating non-compressive perturbations $Vx_{\rm AM}$, $Bx_{\rm AM}$, $Vy_{\rm AM}$, and $By_{\rm AM}$ (lower panels) for the basic case of $\sigma_c = 0.62$. The white dashed lines show the theoretical propagation speed of slow magnetosonic waves and Alfvén waves along the z-direction. The compressive perturbations and non-compressive perturbations are along different slices.

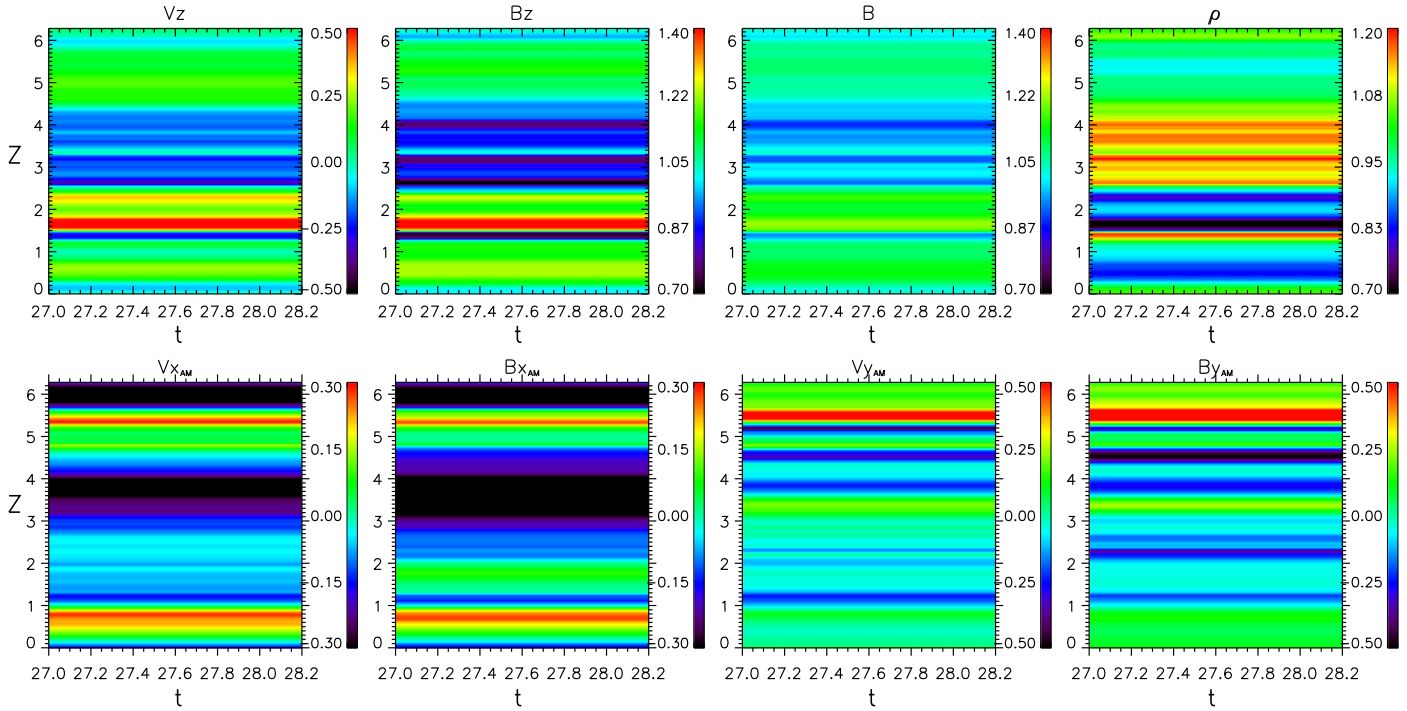

Figure 10. Distance–time ($Z - t$) diagrams of the non-propagating compressive perturbations Vz, Bz, B, and ρ (upper panels) and the non-propagating non-compressive perturbations $Vx_{\rm AM}$, $Bx_{\rm AM}$, $Vy_{\rm AM}$, and $By_{\rm AM}$ (lower panels) along for the basic case of $\sigma_c = 0.62$. The compressive perturbations and non-compressive perturbations are along different slices.

density and the field-aligned component of the magnetic field on the ion plasma beta is consistent with a spectrum of compressible wave energy that is almost entirely in the kinetic slow-mode, indicating that the compressible component of the inertial range solar wind turbulence are primarily kinetic slow modes (Howes et al. 2012; Klein et al. 2012). However, Verscharen et al. (2017) showed that the observations of the slow wave polarization of the solar wind turbulence agree more with the MHD predictions than with those of the kinetic predictions, which suggest that the plasma behaves more like a fluid in the solar wind than expected. Meanwhile, the MHD slow-mode waves are found in the solar wind (Yao et al. 2013b;

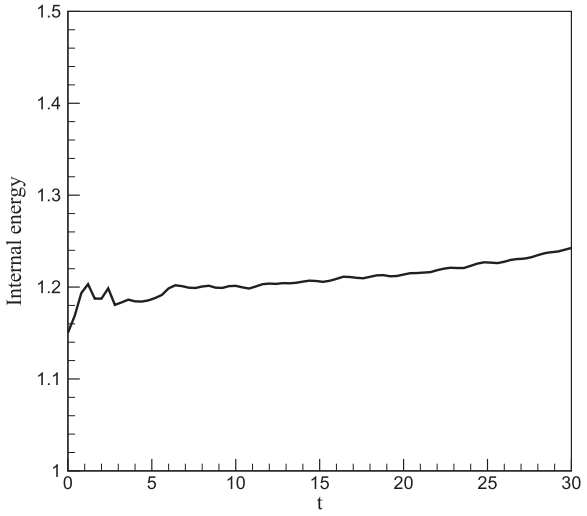

Figure 11. Evolution of internal energy from $t = 0$ to $t = 30$ for the basic case.

He et al. 2015; Shi et al. 2015). As the current model lacks realistic descriptions of kinetic solar wind processes, the slow magnetosonic waves are identified here. Including kinetic descriptions of plasma into numerical models is necessary to see the generation of kinetic slow-mode waves.

Moreover, the damping rate of the actual slow waves is proportional to the parallel component of the wavevector, and for quasi-perpendicular wavevectors, the slow wave corresponds to an undamped, non-propagating PBS (Howes et al. 2006). Here, we find that the quasi-perpendicular slow magnetosonic waves and the non-propagating features coexist in the MHD turbulence. Currently, we have no answer to the question whether the non-propagating features, such as slow-mode structures, originate from the quasi-perpendicular slow-mode waves, although multiscale PBSs are shown to be likely associated with the oblique-propagating slow-mode waves (Yang et al. 2017a).

Also, the nonlinear evolution of the MHD turbulence gives the prevalence of the quasi-perpendicular slow and Alfvén modes. Do the quasi-parallel modes suffer from strong damping, although kinetic damping is out of scope of this work, or can they just not be effectively produced by the energy cascade of the MHD turbulence? For the different cases presented in this work, we make comparisons between several slices from each datacube, which may not be the best way to do it. Devising some statistical measure, such as the bispectrum method (Burkhart et al. 2009), seems necessary to further investigate the interaction versus propagation about waves and structures. At last, it is important to determine the fraction of the volume or energy with propagating and non-propagating perturbations. In future works, we plan to use 4D spatial-temporal (x, y, z, t) Fourier transformations of the whole computational domain to address this question.

This work is supported by NSFC grants under contracts 41774157, 41674171, 41474147, 41731067, 41574168, 41421003, and the Specialized Research Fund for State Key Laboratories. The work was carried out at National Supercomputer Center in Tianjin, China and the calculations were performed on TianHe-1 (A). J.S.H. is also supported by National Young Talent Support Program of China. L.-P.Y, L. Z., and J.-S. H. contributed equally to this work and should be considered as co-first authors.

ORCID iDs

Jiansen He https://orcid.org/0000-0001-8179-417X
Chuanyi Tu https://orcid.org/0000-0002-9571-6911
Linghua Wang https://orcid.org/0000-0001-7309-4325

References

Borovsky, J. E. 2008, JGR, 113, A08110
Brandenburg, A., & Lazarian, A. 2013, SSRv, 178, 163
Bruno, R., & Carbone, V. 2013, LRSP, 10, 2
Bruno, R., Carbone, V., Veltri, P., Pietropaolo, E., & Bavassano, B. 2001, P&SS, 49, 1201
Burkhart, B., Falceta-Gonçalves, D., Kowal, G., & Lazarian, A. 2009, ApJ, 693, 250
Burlaga, L. F. 1968, SoPh, 4, 67
Cho, J., & Lazarian, A. 2002, PhRvL, 88, 245001
Cho, J., & Lazarian, A. 2003, MNRAS, 345, 325
Cho, J., & Lazarian, A. 2005, ThCFD, 19, 127
He, J., Tu, C., Marsch, E., et al. 2015, ApJL, 813, L30
Hnat, B., Chapman, S. C., & Rowlands, G. 2005, PhRvL, 94, 204502
Howes, G. G., Bale, S. D., Klein, K. G., et al. 2012, ApJL, 753, L19
Howes, G. G., Cowley, S. C., Dorland, W., et al. 2006, ApJ, 651, 590
Kellogg, P. J., & Horbury, T. S. 2005, AnGeo, 23, 3765
Klein, K. G., Howes, G. G., TenBarge, J. M., et al. 2012, ApJ, 755, 159
Kowal, G., & Lazarian, A. 2010, ApJ, 720, 742
Kowal, G., Lazarian, A., & Beresnyak, A. 2007, ApJ, 658, 423
Liu, Z.-X., He, J.-S., & Yan, L.-M. 2014, RAA, 14, 299
Marsch, E. 1986, A&A, 164, 77
Marsch, E., & Tu, C. Y. 1993, AnGeo, 11, 659
Narita, Y., & Marsch, E. 2015, ApJ, 805, 24
Passot, T., & Vázquez-Semadeni, E. 2003, A&A, 398, 845
Roberts, D. A., Goldstein, M. L., Matthaeus, W. H., & Ghosh, S. 1992, JGR, 97, 17115
Ruan, W., He, J., Zhang, L., et al. 2016, ApJ, 825, 58
Shi, M., Li, H., Xiao, C., & Wang, X. 2017, ApJ, 842, 63
Shi, M. J., Xiao, C. J., Li, Q. S., et al. 2015, ApJ, 815, 122
Tu, C.-Y., & Marsch, E. 1993, JGR, 98, 1257
Tu, C.-Y., & Marsch, E. 1994, JGR, 99, 21481
Tu, C.-Y., & Marsch, E. 1995, SSRv, 73, 1
Verscharen, D., Chen, C. H. K., & Wicks, R. T. 2017, ApJ, 840, 106
Vestuto, J. G., Ostriker, E. C., & Stone, J. M. 2003, ApJ, 590, 858
Wang, T., Cao, J., Fu, H., Meng, X., & Dunlop, M. 2016, GeoRL, 43, 1854
Yang, L., He, J., Tu, C., et al. 2017a, ApJ, 836, 69
Yang, L., He, J., Tu, C., et al. 2017b, ApJ, 846, 49
Yang, L., Zhang, L., He, J., et al. 2017c, ApJ, 851, 121
Yang, L., Zhang, L., He, J., et al. 2015, ApJ, 809, 155
Yao, S., He, J.-S., Marsch, E., et al. 2011, ApJ, 728, 146
Yao, S., He, J.-S., Tu, C.-Y., Wang, L.-H., & Marsch, E. 2013a, ApJ, 776, 94
Yao, S., He, J.-S., Tu, C.-Y., Wang, L.-H., & Marsch, E. 2013b, ApJ, 774, 59
Yoon, H., Cho, J., & Kim, J. 2016, ApJ, 831, 85
Zank, G. P., Adhikari, L., Hunana, P., et al. 2017, ApJ, 835, 147
Zhang, L., He, J., Tu, C., et al. 2015a, ApJL, 804, L43
Zhang, L., Yang, L.-P., He, J.-S., et al. 2015b, AnGeo, 33, 13
Zhao, J. S., Voitenko, Y., Yu, M. Y., Lu, J. Y., & Wu, D. J. 2014, ApJ, 793, 107